Bioactive Materials 21 (2023) 436–449

Contents lists available at ScienceDirect

Bioactive Materials

journal homepage: www.keaipublishing.com/en/journals/bioactive-materials

Shifting focus from bacteria to host neutrophil extracellular traps of biodegradable pure Zn to combat implant centered infection

Feng Peng [a,1], Juning Xie [a,b,1], Haiming Liu [c], Yufeng Zheng [d,****], Xin Qian [a], Ruixiang Zhou [a], Hua Zhong [e,***], Yu Zhang [a,b,**], Mei Li [a,*]

[a] Medical Research Center, Department of Orthopedics, Guangdong Provincial People's Hospital, Guangdong Academy of Medical Sciences, Guangzhou, 510080, China
[b] School of Medicine, South China University of Technology, Guangzhou, 510006, China
[c] WeiLun PET Center, Department of Nuclear Medicine, Guangdong Provincial People's Hospital, Guangdong Academy of Medical Sciences, Guangzhou, 510080, China
[d] School of Materials Science and Engineering, Peking University, Beijing, 100871, China
[e] Department of Orthopaedics, The Fifth Affiliated Hospital, Southerm Medical University, Guangzhou, 510009, China

ARTICLE INFO

Keywords:
Neutrophil extracellular trap
Antibacterial
Zinc implant
Orthopedic infection

ABSTRACT

The widespread use of orthopedic implants to support or replace bones is increasingly threatened by the risk of incurable bacterial infections, impenetrable microbial biofilms, and irreversible antibiotic resistance. In the past, the development of anti-infective biomaterials focused solely on direct antibacterial properties while ignoring the host's immune response. Inspired by the clearance of infection by the innate neutrophil response and participation in anti-infectious immunity of Zn ions, we report an innovative neutrophil extracellular traps (NETs) strategy, induced by biodegradable pure Zn, which achieved therapeutic efficacy toward biomaterial-related infections. Our *in vitro* and *in vivo* data showed that pure Zn was favorable for NETs formation by promoting the release of DNA fibers and granule proteins in a reactive oxygen species (ROS)-dependent manner, thereby retraining and degrading bacteria with an efficiency of up to 99.5%. Transcriptome analysis revealed that cytoskeletal rearrangement and toll-like receptor (TLR) signaling pathway were also involved in Zn-induced NETs formation. Furthermore, the *in vivo* results of a *Staphylococcus aureus* (*S. aureus*)-infected rat model verified that pure Zn potentiated the bactericidal capability of neutrophils around implants, and promoted osseointegration in *S. aureus*-infected rat femurs. This antibacterial immunity concept lays a foundation for the development of other antibacterial biomaterials and holds great promise for treating orthopedic infections.

1. Introduction

Traditionally, non-degradable materials (such as stainless steel, cobalt-chromium (Co–Cr) alloys, and titanium (Ti) alloys) are widely used as orthopedic implants owing to their good mechanical strength and biocompatibility [1]; however, the mismatched elastic moduli of these implant materials lead to stress shielding, consequent inflammation, and implant loosening [2]. Moreover, these permanent implants often require revision surgery and removal after tissue repair, which might damage the tissue and increase the economic burden of the patients. Biodegradable metals, including magnesium (Mg), iron (Fe), and zinc (Zn), are considered to be the next generation of biomedical implants for their *in vivo* complete degradation; thus eliminating the need for a second surgery [3–6]. Although studies on Mg are the most in-depth among the three metals, its rapid and uncontrollable degradation inhibits its large-scale application to the clinical setting [7,8]. Moreover, the mechanical strength of Mg is the lowest, making it unsuitable for load-bearing implants [3]. The complete degradation time for Fe is 2–3 years, which is relatively long and does not match the repair time of the injured tissues [9]. In addition, the corrosion products of Fe

Peer review under responsibility of KeAi Communications Co., Ltd.
* Corresponding author.
** Corresponding author. School of Medicine, South China University of Technology, Guangzhou, 510006, China.
*** Corresponding author.
**** Corresponding author.
E-mail addresses: yfzheng@pku.edu.cn (Y. Zheng), zhong8099@163.com (H. Zhong), zhangyu@gdph.org.cn (Y. Zhang), limei@gdph.org.cn (M. Li).
[1] These authors contributed equally to this work.

https://doi.org/10.1016/j.bioactmat.2022.09.004
Received 6 July 2022; Received in revised form 23 August 2022; Accepted 5 September 2022

implants, mainly Fe $(OH)_3$ and Fe_3O_4, are not easily excreted or metabolized [10,11]; therefore, more research has focused on the orthopedic application of Zn-based implants, owing to their moderate degradation rate and favorable mechanical properties [12–15]. Furthermore, Zn alloys have been found to modulate osteogenic differentiation and suppress bone tissue loss and inflammatory diseases [16].

Another advantage of Zn-based orthopedic implants is their antibacterial ability [14]. Infection is the main reason for orthopedic implant failure [17]. Even under strict aseptic operative conditions and perioperative preventive anti-inflammatory treatment, the infection rate of periprosthetic tissue is 2–3%, reaching as high as 30% in open fractures. Additionally, repeated and prolonged antibiotic treatment further increases multi-drug resistance [18]. *Staphylococcus aureus* (*S.aureus*) is the main pathogenic bacteria causing bone infection, accounting for about 37.5–58.5% of infectious osteomyelitis [19]. Zn ions are widely used as antibacterial agents, and many biomaterials incorporated Zn to enhance their antibacterial ability [20–22]. For example, our previous study reported that Zn-modified Mg surfaces using hydrothermal treatment or dopamine self-polymerization methods showed superior antibacterial ability [21,23]. The sustained release of Zn ions from Zn-based implants also bestows them with favorable *in vitro* and *in vivo* antibacterial activity through charge transfer, disruption of proton circulation, reactive oxygen species (ROS) production, and protein denaturation. Notably, the cell walls of gram-positive bacteria are more vulnerable to Zn ions, thus, membrane damage further enhances inhibitory activity of Zn towards infection [14,24–26]. In addition to its direct antibacterial effect, Zn has emerging roles as a phagocyte antimicrobial effector [27]. Once a biomaterial is implanted, it first induces immune responses, which then guide the bacterial killing process, followed by the direct antibacterial action of the implant [28,29]; however, most research concerning the antibacterial effect of Zn focus on the final step [30], whereas ignoring its potential immune-mediated antibacterial capabilities.

When bacteria invade bone defects, neutrophils are the first immune cells that migrate to the damaged area in response to chemotactic stimulation from the inflammatory site. Mature neutrophils are fully equipped with granules, which store proteins that enable neutrophils to hit against microorganisms [31]. Subsequently, the antimicrobial defense of neutrophils is achieved by direct phagocytosis and the release of an antibacterial arsenal [28]. Neutrophils can form neutrophil extracellular traps (NETs) by releasing nuclear material outside the cell upon neutrophil activation [32]. The NETs, described as extracellular fibers of DNA and associated proteins, can trap and kill invading bacteria effectively, exhibiting little tissue damage during the antimicrobial defense. NETs also serve as a physical barrier to prevent the spread of bacteria [33] and achieve vascular remodeling [34].

Zn^{2+} acts as a secondary messenger in various immune cells, and the activation of human and mouse T cells or dendritic cells (DCs) is accompanied by an increase in intracellular Zn^{2+} concentration. Furthermore, Zn^{2+} has also been found to participate in anti-infectious immunity, for example, immune cell populations respond to extracellular Zn^{2+} stimuli and initiate intracellular immune signaling via Zn transporters [35]; therefore, Zn^{2+} can activate immune cells and is involved in the innate and adaptive immune responses. More importantly, a Zn deficiency can directly induce functional damage to neutrophils, especially the formation of NETs; however, the regulation of neutrophil activity and NETs formation by Zn or Zn alloys has not been reported. Hence, investigating whether Zn-based implants can kill bacteria by inducing NETs formation is of great importance to the design of Zn-based anti-infection orthopedic implants.

In this study, we used Ti implants as a control group to investigate the ability of Zn implants to induce NETs formation. The underlying cellular and molecular mechanisms were explored using transcriptome sequencing. The *in vivo* antibacterial, immune response, and bone regeneration performances of Zn were systematically studied using bone implantation models.

2. Materials and methods

2.1. Extracts collection

Commercially purchased pure Zn (>99.99%) and Ti (>99.99%) were cut into 10 mm in diameter and 1 mm in height. The samples were immersed in culture medium with a ratio of 1.25 cm^2/mL. After incubated at 37 °C for 24 h, the culture extracts was collected and stored at 4 °C for further use. The Zn^{2+} concentration in the extract of Zn group was 2.92 ± 0.08 ppm detected by inductively coupled plasma optical emission spectrometer (ICP-OES; Thermo Fisher iCAP 7400, USA).

2.2. Neutrophil isolation

All animal experiments were approved by the Institutional Animal Care and Use Committee of Guangdong Provincial People's Hospital (KY-Q-2021-236-01). Mouse bone marrow neutrophils were isolated from femurs and tibias of 10-week-old Balb/c mice using the bone marrow neutrophil isolation kit (Tianjin HaoYang Biological Manufacture Co.Ltd, China). All experimental procedures were carried out according to the manufacturer's instructions and erythrocytes from the marrow isolates were removed using ACK Lysing Buffer. Subsequently, all the isolated neutrophils were grown in 1640 medium (RPMI-1640; Gibco, USA) containing 10% fetal bovine serum (FBS; Gibco, USA) and cultured in a humidified, 5% CO_2 incubator at 37 °C. The purity of naive neutrophils (Ly6G + CD11b+) was verified to be about 90% using flow cytometry (Fig. S1). The viability of the isolated neutrophils was observed using trypan blue staining (Sigma-Aldrich, USA) and found to be greater than 98%.

2.3. In vitro NETs formation analysis

NETs were generated and evaluated as previously described with some modifications to the biomaterials [36]. Briefly, isolated neutrophils were resuspended in sample extracts and approximately 4×10^5 neutrophils per well were seeded onto the 24-well plates for 5 h. The cells activated with 100 nM phorbol 12-myristate 13-acetate (PMA; Sigma-Aldrich, USA) and RPMI 1640 medium were used as positive and negative controls, respectively. Thereafter, the cells were washed and fixed with 4% (w/v) paraformaldehyde (PFA) for 30 min, followed by washing with PBS three times and permeabilization with 0.1% Triton X-100 for 15 min. The circulating free DNA (cfDNA) was stained with SYTOX Green (1 μM; Thermo Fisher Scientific, USA). In a parallel setting, neutrophils were treated with the extracts described above in the presence of the NADPH oxidase (NOX) inhibitor diphenylene iodonium (DPI, 10 μM; Sigma-Aldrich) or DNA digestive enzyme DNase I (20 units/mL) for 30 min. The NETs formation was characterized by the circularity of stained DNA and visualized using a fluorescence microscope.

2.4. NETs quantification

The NETs were quantified using the Quant-iT PicoGreen the double-stranded DNA (dsDNA) assay kit (ThermoFisher Scientific, USA). In brief, 4×10^5 isolated neutrophils were stimulated with Zn and Ti extracts for 5 h. Biomaterial-induced NETs levels were quantified by measuring the fluorescence intensity of extracellular dsDNA released in the culture using a fluorescent microplate reader at an excitation wavelength of 485 nm and an emission wavelength of 535 nm. The NETs formation of neutrophils treated with the extracts described above in the presence of DPI (10 μM; Sigma-Aldrich) or DNase I (20 units/mL) for 30 min was also detected.

2.5. Myeloperoxidase-DNA (MPO-DNA) complex detection

MPO-DNA was detected using a previously described sandwich

enzyme-linked immunosorbent assay (ELISA) protocol with slight modifications [37]. Briefly, 4×10^5 isolated neutrophils were stimulated with Zn and Ti extracts for 5 h. A mouse anti-MPO monoclonal antibody (R&D Systems, USA) was used as a capture antibody (5 μg/mL) and coated on a 96-well microplate. After blocking with 1% bovine serum albumin (BSA), the cell culture supernatant, together with a peroxidase-labelled anti-DNA monoclonal antibody, was added (Roche, Germany) and incubated for 2 h. The peroxidase substrate was added, and the absorbance was measured at 405 nm using a microplate reader (Thermo Fisher Scientific, USA).

2.6. Immunofluorescence staining

Mouse neutrophils were isolated and seeded (5×10^4 cells/well) onto the 24-well plates to induce NETs formation as described above. After fixation with 4% PFA for 30 min, the cells were permeabilized with 0.1% Triton X-100 for 20 min and blocked with a protein-free rapid blocking buffer (Shanghai Epizyme Biomedical Technology Co, China). Subsequently, the cells were immune-stained with a primary monoclonal anti-citrullinated-histone H3 (CitH3, 1:100, rabbit, Abcam) antibody overnight at 4 °C, followed by detection with an Alexa Fluor 594 goat anti-rabbit IgG H&L (1:500, Abcam) secondary antibody for 1 h. The samples were mounted with DAPI (10 ng/mL; Sigma-Aldrich, USA) for DNA detection. Fluorescence images were obtained using a fluorescence microscope.

2.7. In vitro antibacterial and bacterial immune evasion assays

Gram-positive bacteria (*S. aureus*, ATCC 25293) were used as model bacteria in the *in vitro* antibacterial tests. *S. aureus* was selected from single colonies on nutrient agar plates and grown overnight in a sterile nutrient broth. The overnight bacterial growth culture was diluted, and the concentration was adjusted to 2×10^6 cfu/mL, according to the McFarland turbidimetry method. The antibacterial activity against *S. aureus* was determined using the plate-counting method. In brief, sterilized pure Zn and Ti discs were placed on the bottom chamber of the transwell plate, and 500 μL of bacterial suspension was added to the upper chamber of the transwell and incubated for 24 h at 37 °C. The planktonic bacteria in the obtained suspensions were then diluted and spread onto agar plates. The plates were incubated at 37 °C for 18 h, after which photos were taken, and the colonies were counted. Meanwhile, the cell walls of bacteria were lysed using lysozyme, and the total RNA of *S. aureus* was extracted with a HiPure Bacterial RNA Kit according to the manufacturer's instructions (Magen Biotechnology). Immune evasion-related gene expression was determined using reverse transcription-polymerase chain reaction (RT-PCR) and SYBR Green Master Mix (Trans, China), and 16sRNA was chosen as the internal reference gene. The primer sequences are listed in Table S1, and genes quantification analysis was performed using the $2^{-\Delta\Delta Ct}$ method. To study the *in vitro* bactericidal effect of Zn-induced NETs, neutrophils were introduced into the above culture system (MOI = 10) for the spread plate assay; the difference in the antibacterial effects after blocking NETs by DNase I were also simultaneously compared.

2.8. Transcriptome sequencing analysis

RNA sequencing was employed to detect the RNA expression profiles of NETs formation in the different samples. Briefly, approximately 4×10^5 neutrophils per well were seeded onto the 24-well plates and cultured with Zn and Ti extracts for 5 h. Total RNA was extracted using the TRIzol reagent (Invitrogen, USA). RNA integrity was assessed using a Bioanalyzer 2100 (Agilent, CA, USA) with an RNA Integrity Number (RIN) number >7.0. The acquired samples were then subjected to 2 × 150 bp paired-end sequencing (PE150) on an illumina Novaseq™ 6000 platform (LC-Bio Technology CO., Ltd., China) following the manufacturer's protocol. HISAT2 was used to map the reads to *Homo sapiens* GRCh38 reference genome. The counts and fragments per kilobase million (FPKM) of the aligned genes were assembled using StringTie. The "edgeR" R package was used to analyze the differentially expressed genes (DEGs) using pair-wise comparisons, and differentially expressed mRNAs were selected with a fold change >2 or < 0.5. Gene ontology (GO) analysis and kyoto encyclopedia of genes and genomes (KEGG) enrichment were performed using DAVID tools.

2.9. Detection of ROS

The level of Zn-induced ROS during NETs formation was detected by 2′,7′-dichlorodihydrofluorescein diacetate (DCFH-DA, Beyotime Biotechnology, China). In brief, the neutrophils stimulated with pure Zn or Ti extracts in the presence and absence of DPI for 5 h were incubated with 10 μM DCFH-DA for 30 min at 37 °C. Subsequently, the residual probes were removed, and dichlorofluorescein oxidized by intracellular ROS was detected by fluorescence microscope. Additionally, the intracellular fluorescence intensity was relatively quantified by a fluorescent microplate reader with excitation at 485 nm and emission at 535 nm.

2.10. NOX activity

NOX activity was measured using a colorimetric method according to the manufacturer's instructions. Briefly, isolated neutrophils were stimulated with Zn or Ti extracts for 5 h as described above. Then, neutrophils were lysed with 0.5% Triton X-100 in the presence of 0.2 mM phenylmethylsulfonyl fluoride (PMSF), and the supernatant was collected by centrifugation at 15,000 g for 5 min. The subcellular NOX catalyzed the NADPH substrate in the presence of the specific diphenyleneiodonium inhibitor and formed $NADP^+$, and the enzyme activity was determined using the substrate color, which was measured at 450 nm using a microplate reader.

2.11. Western blotting

For immunoblot analysis, the total intracellular protein was lysed in a radio immunoprecipitation assay (RIPA) buffer containing a proteinase inhibitor cocktail. Next, 25 μg total extracted protein was subjected to 10% sodium dodecyl sulfate–polyacrylamide gel and the gels were transferred to polyvinylidene fluoride (PVDF) membranes. After the transfer, the membranes were blocked with 5% (w/v) BSA for 1 h and then incubated with anti-NOX2 (1:1000, abcam), anti-NOX4 (1:1000, abcam), anti-peptidylarginine deiminase 4 (anti-PAD4; 1:1000, abcam) and β-actin (1:1000, abcam) primary antibodies at 4 °C overnight, followed by incubation with horseradish peroxidase (HRP)-conjugated secondary antibody (1:10000, Thermo Fisher Scientific, USA) for 1 h. Finally, immunoreactive signals were detected through a chemiluminescent reaction using a gel imaging system (ChemiScope 2850, Clinx Science, China) and analyzed by Image J software.

2.12. In vitro osteogenesis evaluation

Rat bone marrow mesenchymal stem cells (rBMSCs) were purchased from Cyagen Biosciences Inc. and cultured in OriCellTM RMSC Complete Media (Cyagen Biosciences, China). The cells (5×10^4/well) were seeded in 24-well plates for 24 h. Thereafter, the culture medium was replaced with Zn and Ti extracts. After cultured for another 24 h, the cells were fixed with 4% paraformaldehyde, permeabilized with Triton X-100, and finally stained with rhodamine phalloidin (KGMP0012, KeyGEN BioTECH, China) and 4′,6-diamidino-2-phenylindole (DAPI) according to the manufacturer's protocols. The cells were observed using a laser scanning confocal microscope (LSM900, Zeiss, Germany).

The cells (5×10^4/well) were seeded in 24-well plates for 24 h. Thereafter, the culture medium was replaced with Zn and Ti extracts containing 10 mM β-glycerophosphate, 50 mM ascorbic acid and 100 nM dexamethasone. After cultured for another 7 and 14 days,

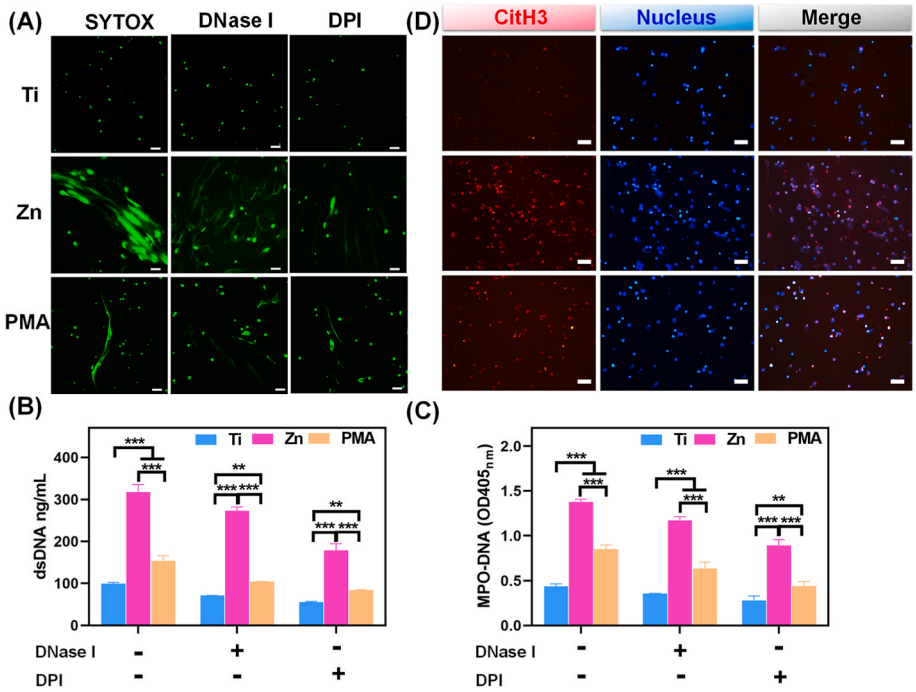

Fig. 1. *In vitro* NETs formation. (A) NETs structures stained by SYTOX Green with and without DNase I and DPI stimulation in different sample extractions (scale bar = 50 μm); PMA (100 nM) was used as a positive control. (B) Quantitative determination of dsDNA in the supernatant of neutrophils, and (C) MPO-DNA complexes levels quantified by ELISA with and without DNase I and DPI stimulation (**: $p < 0.01$; ***: $p < 0.001$). (D) Immunofluorescent images of CitH3 (NETs marker, red) expression in neutrophils cultured in different groups (scale bar = 50 μm).

intracellular alkaline phosphatase (ALP) was stained using the BICP/NBT ALP color development kit (Beyotime, China) and the activity of ALP was measured by ALP assay kit (Beyotime, China) according to the manufacturer's instructions. Total protein concentration was detected using BCA protein assay kit (Beyotime, China) to normalize the ALP level. Meanwhile, the formation of calcium nodules after cultured for 14 days was determined by alizarin red S (ARS) staining. In brief, the cells were fixed with 75% ethanol and then stained with 40 mM Alizarin Red solution (LEAGENE BIOTECHNOLOGY, China). The stained cells were imaged under the microscope (Nikon TI-S, Japan). Thereafter, 10% cetylpyridinium chloride (SigmaAldrich, USA) was added for semi-quantitative analysis of mineralized extracellular matrix (ECM).

2.13. NETs formation, antibacterial capability, and osseointegration in vivo

Twenty-four male Sprague-Dawley rats with an average weight of 200 g were purchased from the Medical Experimental Animal Center of Guangdong Province and randomly divided into Ti (uninfected), Zn (uninfected), Ti (infected) and Zn (infected) groups. Before surgery, the animals were anesthetized with 4% chloral hydrate (0.3 mL/100g). Both lower limbs were shaved, and the surgical site was disinfected for each rat; an incision was made around the knee, exposing the lateral femoral condyle. A hole (2 mm in diameter) was drilled along the direction of the medullary cavity at the center of the femoral condyle. In the infected groups, cylindrical samples (2 mm in diameter and 5 mm in length) immersed in an *S.aureus* suspension (1×10^6 cfu/mL) were implanted into the bone canal. Finally, the wound was disinfected and sutured. The rats were sacrificed using an overdose of pentobarbitone 3 days after the surgery, and the implanted pillars were harvested and rolled over on blood agar plates; these plates were incubated for 18 h at 37 °C to quantify the viable bacteria adhered to the pillars. The femurs with implants were also collected and fixed in 4% PFA, followed by decalcification in EDTA decalcifying solution for 4 weeks, after which the implants were removed from the femurs. The decalcified femurs were then dehydrated, embedded, and sectioned at 5 μm for hematoxylin and eosin (H&E) and Giemsa stainings. The sections were also subjected to immunofluorescent staining with anti-Ly6G (1:1000, biorbyt) and anti-CitH3 (1:1000, abcam), followed by detection with Alexa Fluor 594 goat anti-rabbit IgG H&L (1:500, Abcam) and Alexa Fluor 488 goat anti-rabbit IgG H&L (1:500; Abcam) sectionary antibodies.

To evaluate the bone-to-implant osteointegration, the animals were euthanized 2 months after implantation. The femurs with implants were scanned using a micro-CT system (Inveon™ Multi-Modality; Siemens Medical Solutions, Germany). Three-dimensional (3D) images were reconstructed using multimodal 3D visualization (Siemens Medical Solutions, German) software, and the bone volume to total bone tissue volume (BV/TV) and bone mineral density (BMD) values were calculated using the VG Studio MAX software. The harvested femurs were dehydrated and embedded in polymethylmethacrylate (PMMA). The tissues were sectioned and polished to a thickness of approximately 50 μm. Van Gieson's (VG) staining was then performed on the sections, and representative pictures were acquired. The decalcified sections were processed for H&E staining and immunohistochemistry staining of vascular endothelial growth factor (VEGF), osteocalcin (OCN), osteopontin (OPN). Finally, the positive protein expression was detected by 3,3′-diaminobenzidine solution (Dako, Denmark) and hematoxylin counterstaining, and imaged using a Pannoramic Digital Slide Scanner (3DHISTECH, Hungary).

2.14. Data analysis

All the *in vitro* studies were performed at least 4 repeats. Data are presented as the mean ± standard deviation. Differences among groups were analyzed by one-way and two-way ANOVA followed by Tukey's post hoc test using the SPSS 19.0 software. $P < 0.05$ was considered a significant difference.

3. Results and discussion

3.1. Pure Zn induces NETs formation

The special structure of NETs is characterized as an extracellular DNA scaffold comprising cytoplasmic histones and granule proteins, and this process is defined as "suicidal" NETosis. The web-like structures allow NETs to trap different bacteria efficiently, enabling their clearance

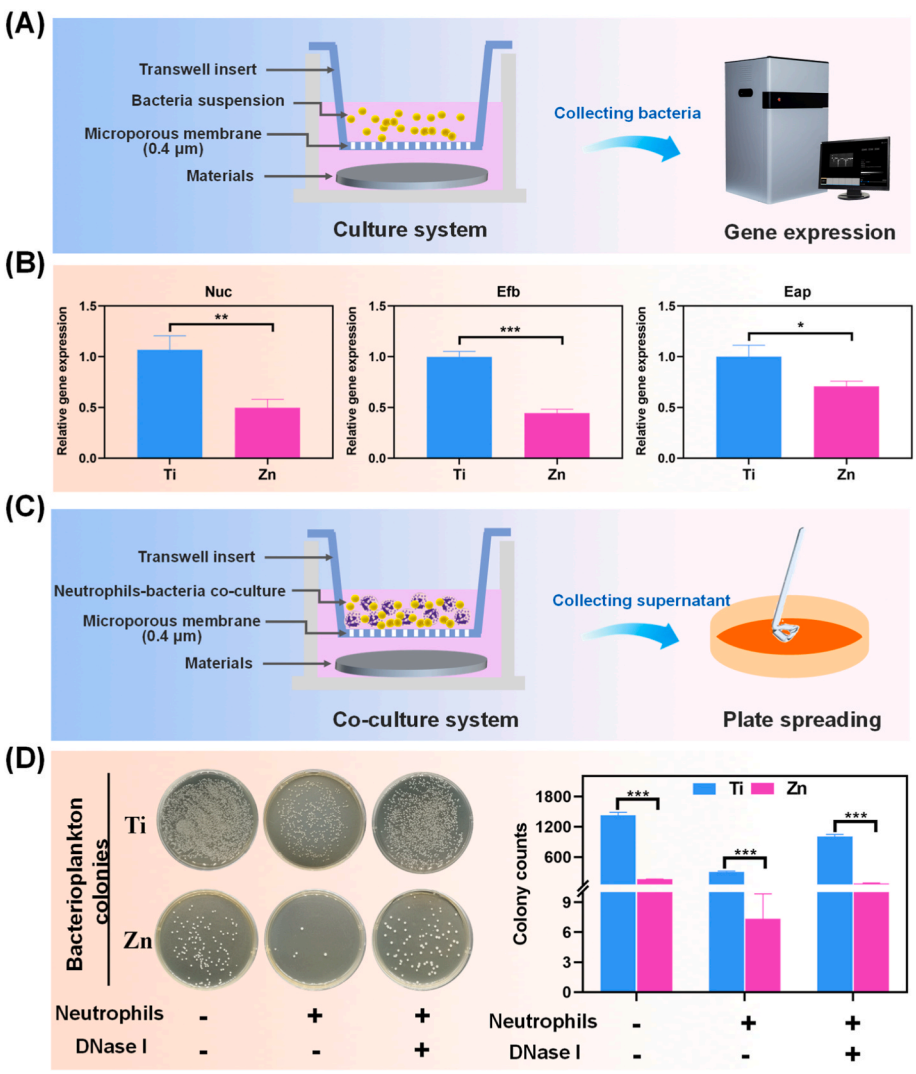

Fig. 2. (A) Scheme of the bacteria culture for PCR detection. (B) Relative *in vitro* mRNA expression of immune evasion-associated genes in *S.aureus* treated with different samples (*: $p < 0.05$; **: $p < 0.01$; ***: $p < 0.001$). (C) Scheme of the co-culture system for plate spreading. (D) Representative culture images of bacterial colonies of *S.aureus* in different groups treated with and without neutrophils or DNase I, and the corresponding counted numbers of *S.aureus* colonies. (***: $p < 0.001$).

by effector molecules, such as proteases and defensins [38]. NETs formation induced by pure Zn was stained with SYTOX Green, and PMA stimulation was used as a positive control. SYTOX Green is an excellent green-fluorescent nucleic acid and chromosome counterstain that is impermeant to live cells, making it a useful indicator of dead cells or cell-free DNA. PMA is a classical stimulus for NETs release by inducing the loss of chromatin density and fusion of nuclear membranes with organelles. As shown in Fig. 1A, PMA-stimulated neutrophils exhibited long, narrow fibrous strands; however, large-scale of net-like structures with strong green fluorescence were observed under Zn extract stimulation, indicating that the pure Zn extract could induce neutrophils to release DNA into the extracellular medium (ECM). When treated with DNase I or DPI, SYTOX Green signals were decreased and the net-like structures were disrupted in the Zn and PMA groups (Fig. 1A), which suggested that the main component of the observed network was DNA and the formation of Zn-induced NETs was closely related to NOX activity.

Furthermore, dsDNA in the supernatants of the above culture system was quantitatively measured using the PicoGreen dsDNA assay kit. As shown in Fig. 1B, DNase I and DPI markedly down-regulated dsDNA level of neutrophils in the Ti, Zn, and PMA groups, confirming NETs depolymerization. However, the Zn and PMA groups showed higher amounts of dsDNA than the Ti group regardless of the addition of DNase I and DPI, further confirming the existence of cell-free DNA in the Zn and PMA groups. The detection of dsDNA released by NETs is fast, simple, and less specific. NETs remnants are usually in the complexes form of cfDNA scaffolds and neutrophil-derived MPO; therefore, MPO is also required for NETs formation, and NETosis is abrogated in patients completely deficient in MPO. By comprehensively considering the structural characteristics of NETs, MPO-DNA complexes can be detected by a modified ELISA protocol, which is the most specific and objective assay for monitoring NETs formation [37]. The analysis of corresponding absorbance characteristics confirmed that the MPO-DNA levels were in the order Zn > PMA > Ti, regardless of whether DNase I or DPI was added (Fig. 1C). CitH3 is a specific biomarker for NETosis and mainly causes chromatin decondensation and then triggers NETs formation to capture microorganisms [39]. In agreement with the results of SYTOX Green staining, as well as dsDNA and MPO-DNA levels, we detected significantly positive CitH3 signals (red fluorescence) in the pure Zn group but very low levels in the Ti group (Fig. 1D). The above results suggested that pure Zn could induce citrullinated modification of histones and intracellular chromatin depolymerization in neutrophils at the infection site, thereby activating the formation of NETs to induce an immune response against infection.

3.2. Pure Zn promotes NETs-associated antibacterial activity

As the most prominent circulating leukocytes in humans, neutrophils invade and accumulate at the infected sites to against pathogens; however, recent studies have found that pathogens have evolved numerous

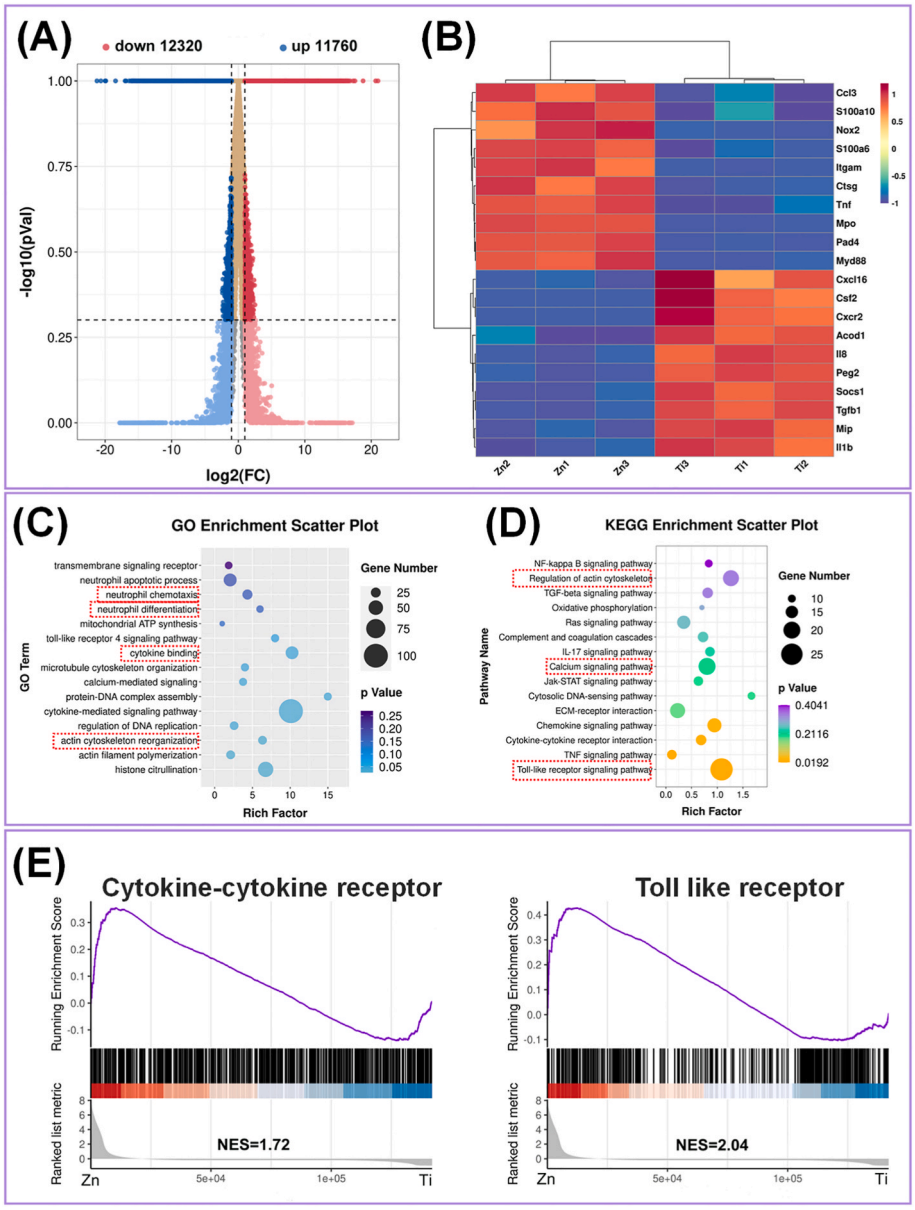

Fig. 3. (A) Volcano plot illustrating expression of DEG from RNA-seq analysis between Ti and Zn. (B) Heatmap of the DEGs related to the neutrophil response in the top 10 up- or down-regulated genes of Ti vs Zn. (C) GO functional clustering and (D) KEGG pathway analysis. (E) The gene set enrichment analysis of the regulated gene pathways with the KEGG and Genomes database.

immune evasion strategies to resist initial acute immune responses, resulting in necrosis of the infiltrated neutrophils. For instance, Preissner KT et al. demonstrated that the extracellular adherence protein (Eap) secreted by *S.aureus* inhibited neutrophil extravasation to the infection sites by directly binding to the intracellular adhesion molecule 1 (ICAM-1) [29,40]. Nuclease (Nuc) plays an important role in immune cell death and breakdown of NETs formation, thus helping *S.aureus* avoid trapping extracellular fibers and antimicrobial peptides [41]. In addition, extracellular fibrinogen-binding protein (Efb) can camouflage bacteria using fibrinogen, which shields them from recognition by the phagocytic receptors on the neutrophils, and further leads to bacterial clumping and quorum sensing [42]. Thus, the study of bacterial immune escape is important to understand the immune efficacy of biomaterials against infection. In the present study, the expression of immune evasion-related genes was detected by RT-PCR (Fig. 2A), and the results shown in Fig. 2B depicted that the expression levels of neutrophil Eap, Efb, and Nuc were down-regulated significantly in the Zn group compared to those in the Ti group ($p < 0.05$). The above results suggested that pure Zn decreased the expression of immune evasion factors, further avoiding the reduction of neutrophil-mediated bactericidal activity as a result of immune escape.

The Zn-mediated reduction in *S. aureus* immune evasion could contribute to NETs formation around the infected microenvironment; however, whether the antibacterial effect of pure Zn is reinforced by NETs formation remains unclear. Herein, an innovative co-culture system of material-neutrophils-bacteria was constructed to investigate the effects of Zn, as shown in Fig. 2C, and plate spreading was conducted to detect the antibacterial ability of NETs and Zn^{2+} together. Fig. 2D shows the qualitative and quantitative results of the antibacterial ability of Ti and Zn extracts treated with or without neutrophils. When bacteria were cultured without neutrophils and DNase I, the Zn group showed fewer bacterial colonies than the Ti group, which can be ascribed to the natural antibacterial property of Zn^{2+}. Both the Ti and Zn groups showed a decrease in the number of bacterial colonies when bacteria were co-cultured with neutrophils. Notably, only a few bacterial colonies were observed for the Zn group, which is likely due to the synergistic

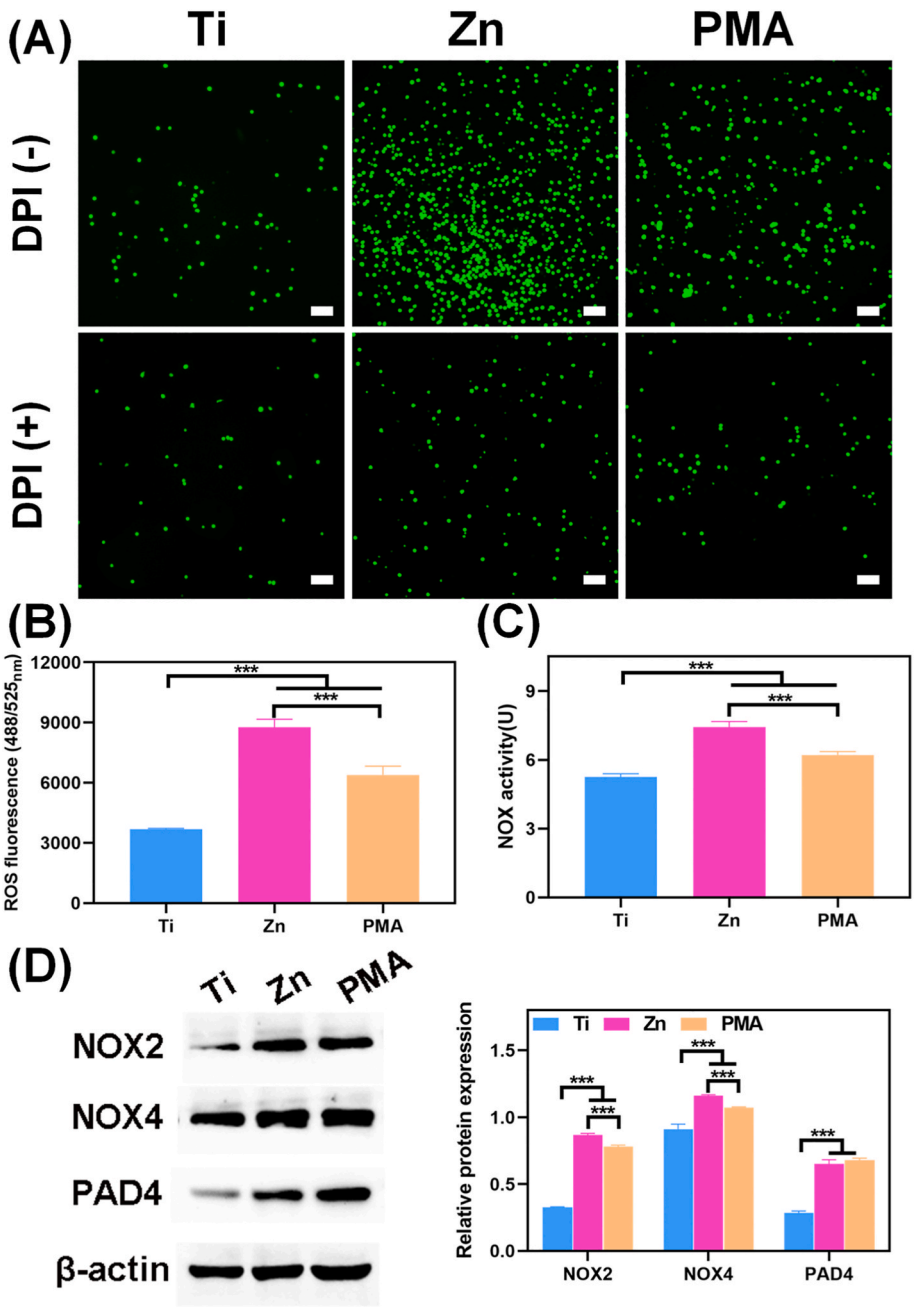

Fig. 4. (A) The fluorescence microscopy images of ROS generation in neutrophils treated by different samples with and without DPI stimulation (scale bar = 50 μm). (B) ROS production in neutrophils was determined using a fluorescence microplate. (C) The quantitative results of NOX activity of neutrophils cultured on different samples for 5 h. (D) Immunoblotting of ROS generation-related proteins (NOX2, NOX4, and PAD4) and the corresponding analysis of their protein expression levels. (***: $p < 0.001$).

bactericidal effect of neutrophils and Zn^{2+}. Additionally, it is worth mentioning that the chromatin and histones in the nucleus have intrinsic antibacterial activity. DNA acts as a cationic chelator and disrupts internal and external bacterial membranes, while histones destroy virulence factors and exhibit a broad-spectrum bactericidal activity [43]. Therefore, the extracellular release of DNA and histones during Zn-induced NETs formation further enhanced the antibacterial effect of Zn^{2+} itself. However, when DNase I was added, the NETs structures in the above system enzymatically polymerized, and the number of bacterial colonies in both groups increased, suggesting that NETs formation by neutrophils was favorable for the antibacterial property of pure Zn. The above results demonstrated that Zn shows natural antibacterial ability and further cooperates with neutrophils in the infectious microenvironment to form NETs, which can almost completely kill the bacteria by degrading virulence factors.

3.3. *Transcriptome and signaling pathway analysis reveals the effects of Zn*

A transcriptomic approach was used to identify the DEGs in neutrophils treated with the Ti and Zn extracts. Good clustering of the detected groups was verified by high Pearson's correlation values (>0.9; Fig. S2A). The violin plot of the coefficient of variance (CV) showed good repeatability between the biological samples (Fig. S2B). Compared with the Ti group, the number of up- and down-regulated genes in neutrophils cultured with the Zn extract was 12320 and 11760, respectively (Fig. 3A). The heat map of the top 10 up- and down-regulated genes is shown in Fig. 3B. Compared to the Ti group, the Zn group showed significantly higher expression of genes, including C–C motif chemokine ligand 3 (Ccl3), S100 calcium binding protein A10 (S100a10), tumor necrosis factor (TNF), myeloid differentiation primary response gene 88 (Myd88), NOX2, MPO, and PAD4. Among them, Ccl3

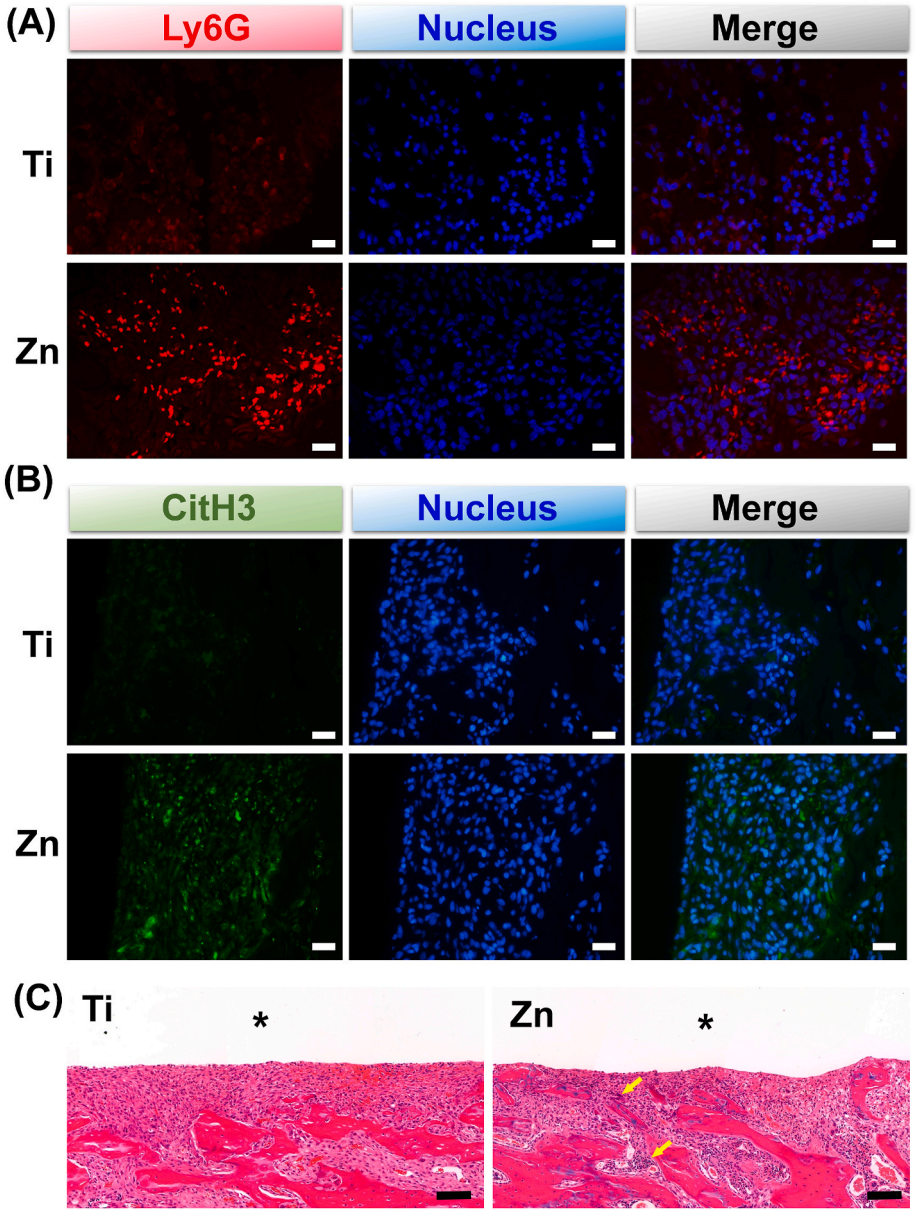

Fig. 5. Immunofluorescence images of (A) Ly6G (Neutrophils marker, red) and (B) CitH3 (NETs marker, green) in bone tissues (scale bar = 100 μm). (C) Histological evaluation of bone tissues adjacent to different implants on day 3 after implantation (scale bar = 100 μm). Asterisks represent the implants. Yellow arrows indicate neutrophils.

and TNF act as chemokines, which orchestrate the recruitment of neutrophils from the blood to infection sites [44]. S100a10 is a small Ca-binding protein that highly expressed during neutrophil activation. A recent study showed that S100a10 is a newly discovered marker of NETs release [45]. Previous studies have reported that NOX2 is responsible for ROS production, while cytosolic or mitochondrial ROS promotes the release of neutrophil elastase and MPO from granules, leading to PAD4 activation [46]. PAD4 is another key molecule during NETs formation that catalyzes the deamination of histones, converting arginine residues into citrulline [47]. Therefore, the gene expression data suggested that pure Zn up-regulated the expression of genes associated with NETs formation and antibacterial behavior.

The GO enrichment scatter plot indicates the classification of gene functions at the molecular and cellular levels. As shown in Fig. 3C, the top 15 GO terms of pure Zn were related to the regulation of neutrophil chemotaxis and differentiation, cytoskeleton organization, and cytokine signaling in the biological process analysis. A larger rich factor represents higher degree of GO enrichment. To further understand the signaling pathways involved in regulating neutrophil differentiation and proinflammatory responses, the KEGG pathway analysis was performed to determine the corresponding pathways. The scatter plot (Fig. 3D) revealed that the regulation of the actin cytoskeleton, Ca signaling pathway, and Toll-like receptor (TLR) signaling pathway (indicated by red dotted box), were highly enriched. Waterman et al. found that neutrophils exhibited rapid disassembly of the actin cytoskeleton and remodeling of microtubules upon NETosis. Inhibition of actin disassembly blocked discharge of extracellular DNA and NET release [47]. Ca influx has been reported to be dependent for NETs formation during mitochondrial ROS production [48]. TLR, specifically, TLR2 and TLR4, are key mediators of innate immunity and inflammation through the identification of pathogen-associated molecular patterns (PAMPs) and activation of the intracellular Myd88 pathway. The absence of TLR2 or TLR4 limits the infiltration of neutrophils into the infection sites by dampening chemokine receptor expression. Additionally, the combined

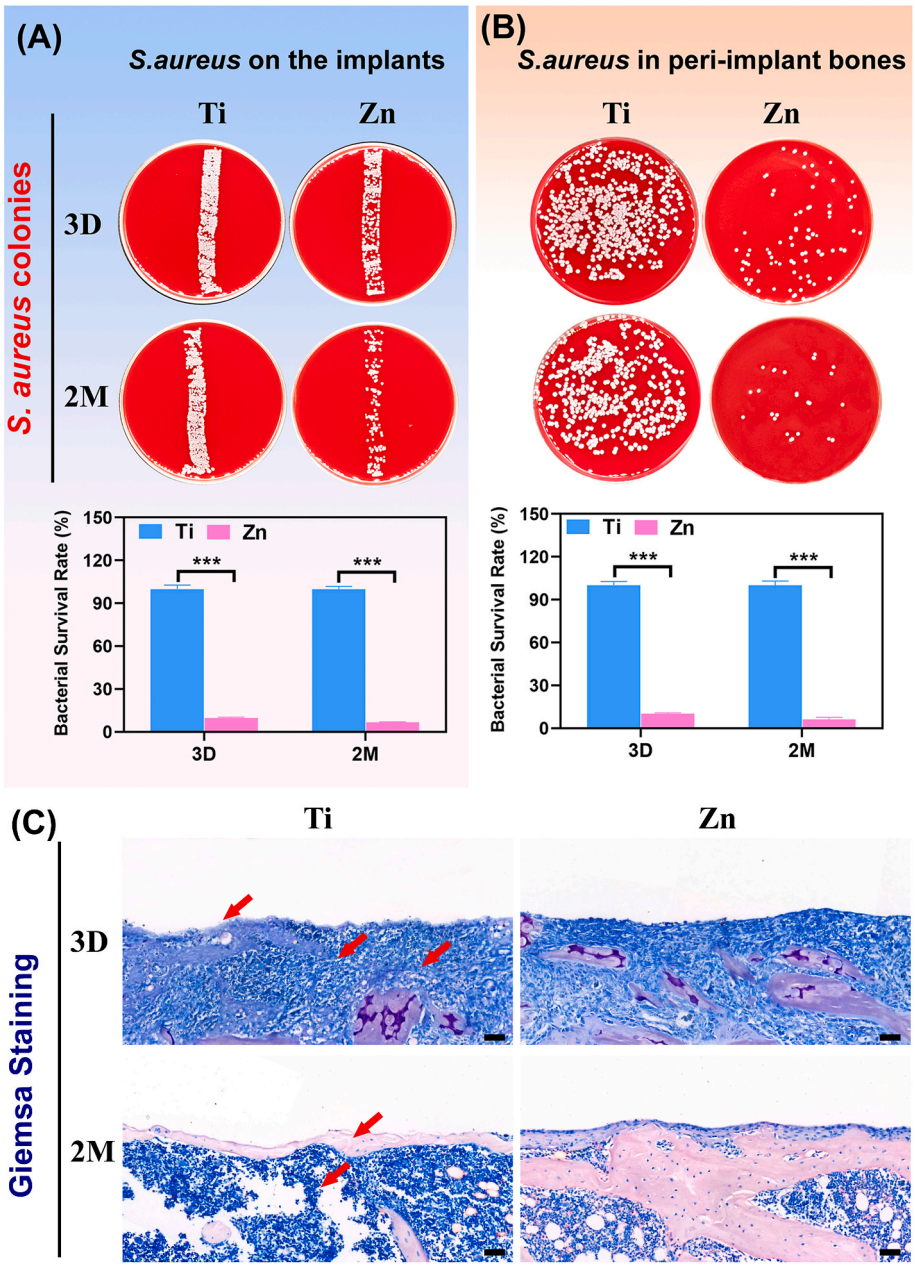

Fig. 6. The antibacterial performance in *S.aureus*-infected femurs. Representative culture images of *S. aureus* colonies formed by (A) rolling the implanted pillars and (B) spreading the peri-implant bone tissues on blood agar plates on 3 days and 2 months after surgery (***: $p < 0.001$). (C) Giemsa staining of the decalcified tissue sections around the implants (scale bar = 100 μm). Red arrows indicate bacteria.

requirement of TLR-mediated opsonization tightly regulates NETs release [49]. In line with these findings, our results indicated that pure Zn-induced NETs formation occurred by cytoskeleton- and TLR-dependent mechanisms.

Gene set enrichment analysis was also applied to investigate the relevant signaling pathways (Fig. 3E). It was found that cytokine receptor (NES = 1.72) and TLR (NES = 2.04) signaling pathways were positively regulated in the Zn group, which also indicated that the two signaling pathways participate in the regulation of neutrophil behavior. In addition, the NES results demonstrated that Ca pathway, chemokine pathway, ECM receptor interaction, janus kinase-signal transducers and activators of transcription (JAK-STAT) pathway, actin cytoskeleton, and transforming growth factor-β (TGF-β) pathway were significantly influenced by the Zn extract (Fig. S2C), which were consistent with the KEGG pathway analysis.

3.4. Pure Zn-induced NETs formation is NOX/ROS signaling-dependent

DCFH-DA was used to evaluate the intracellular ROS expression in neutrophils under pure Zn treatment. The staining images and calculated fluorescence intensities are shown in Fig. 4A and B, respectively. The results suggested that neutrophils cultured in the PMA and Zn groups, especially in the Zn group, generated more intracellular ROS than those in the Ti group. Previous reports have shown that ROS induces NETosis by oxidizing DNA and initiating DNA repair; thus, inhibiting the ROS generation could prevent NETs formation in response to PMA stimulation [50]. However, whether the presence of ROS is necessary for Zn-induced NETs formation requires further investigation and discussion.

ROS are primarily produced by NOX, which can transport electrons across the plasma membrane and generate superoxide and other downstream ROS [51]. Cytosolic or mitochondrial ROS production leads

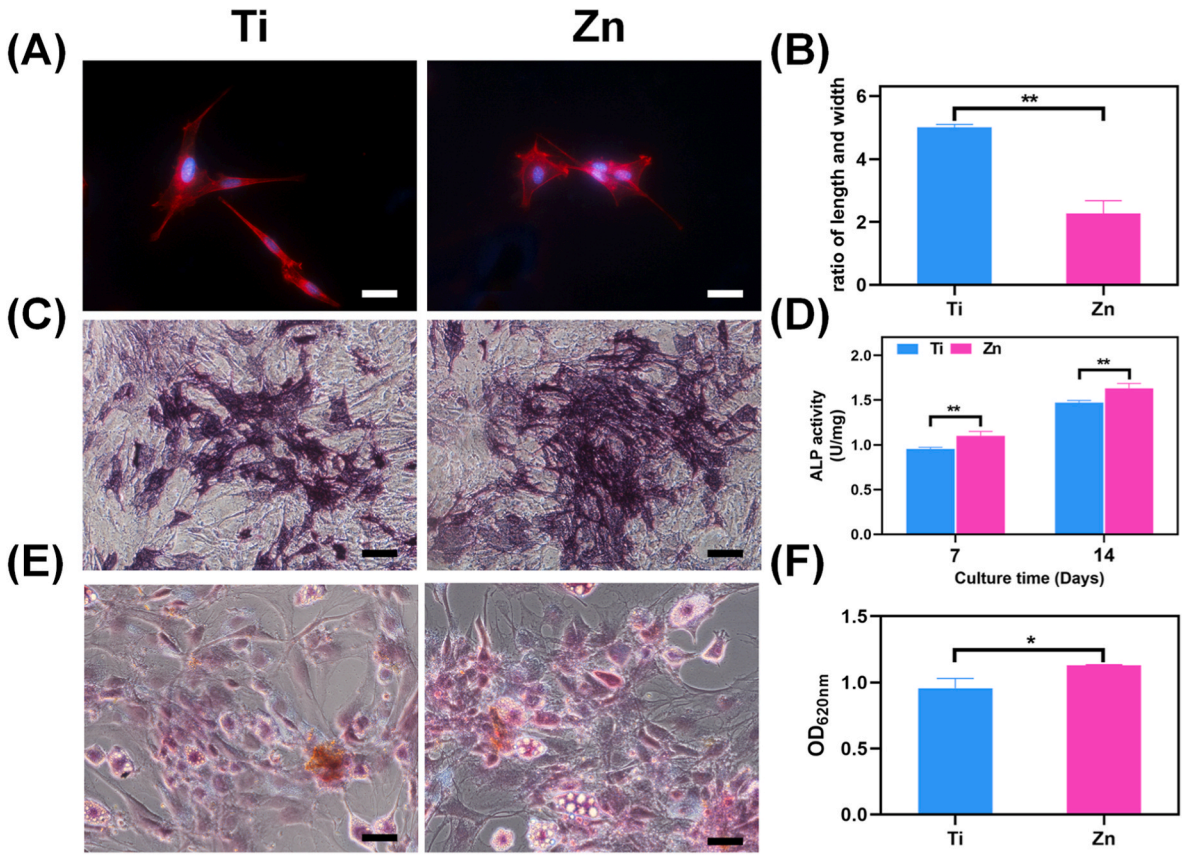

Fig. 7. (A) Cytoskeleton of rBMSC cultured in different extracts and (B) the corresponding aspect ratios calculation (scale bar = 50 μm, **: $p < 0.01$). (C) ALP staining for 7 days and (D) quantitative analysis of the ALP activity for 7 and 14 days (scale bar = 100 μm, **: $p < 0.01$). (E) ARS staining and (F) quantitative analysis of the ECM mineralization in rBMSCs cultured for 14 days (scale bar = 100 μm, *: $p < 0.05$).

to MPO release and PAD4 activation; therefore, the NOX activity of Zn-treated neutrophils was also detected using colorimetric method and western blotting. As shown in Fig. 4C, NOX activity followed the same trend as ROS expression. The protein expression of NOX2, NOX4, and PAD4 in neutrophils cultured in the Zn and PMA groups was higher than that in the Ti group (Fig. 4D). This finding was consistent with the verified the transcriptome analysis results. However, when neutrophils were co-cultured with DPI, a widely used NOX inhibitor that interacts with the catalytic subunit, all three groups generated similar intracellular ROS levels (Fig. 4A), which, in turn, explained the depolymerization effect of DPI on NETs formation (Fig. 1A). Together, these data suggested that NOX2-and NOX4-induced ROS expression plays an important role in NETs formation.

3.5. *In vivo NETs induction and anti-infection effects of pure Zn*

The *in vivo* immune response and antibacterial activity of Zn were evaluated using a rat model of implant-associated infection. Bone tissues surrounding the implants were decalcified and subjected to immunofluorescence and H&E. As shown in Fig. 5A, more immunofluorescence-stained Ly6G (red fluorescence, a marker for myeloid neutrophils) was observed in the Zn group on day 3 after implantation, suggesting that Zn was more beneficial for the recruitment of neutrophils. Moreover, CitH3 immunofluorescence observed in the Zn group suggested that the recruited neutrophils could form more NETs surrounding the Zn implant (Fig. 5B). H&E staining showed more neutrophils (indicated by yellow arrows) surrounding Zn implants, indicating more serious acute inflammation and better bacterial elimination (Fig. 5C, high magnification shown in Fig. S3A).

The implant samples were collected to roll over the blood plate, and peri-implant bones were also collected for plate colony counting on day 3 and month 2 after implantation. Fig. 6A and B show photographs of *S. aureus* colonies formed by rolling the implants and plating the diluted solution from peri-implant bone tissues on blood plates, respectively. The corresponding bacterial survival rate (%) was calculated. Significantly fewer bacteria were observed on the Zn implants and within the peri-implant bone, whereas many bacterial colonies were isolated from the Ti implants and the surrounding bone tissues on day 3 and month 2 postoperatively. Therefore, the *in vivo* and *in vitro* antibacterial activity of Zn implants was consistent. Giemsa staining was performed to observe the infection of the bone tissues surrounding the implants through decalcified tissue sections. As shown in Fig. 7C (high magnification shown in Fig. S3B), the Ti group exhibited the presence of higher number of bacteria (indicated by the red arrows) than the Zn group at both time points. These results suggested that Zn could better reprogram *in vivo* neutrophil behavior to kill bacteria.

Neutrophils are essential cells of the immune system that respond immediately to invading microbes; they are also specialized to the innate immune response, with the ability to eliminate pathogens through phagocytosis and NETs [52]. Zn induces signal transduction in several immune cells, including inflammatory and immune signaling. Additionally, Zn levels are closely correlated with the intensity of the immune response, especially those induced by neutrophils. Freshly isolated human neutrophils were found to be rich in Zn in comparison to other metal ions [53]. Haase et al. demonstrated that Zn signals were essential for ROS-dependent signal transduction leading to NETosis, because NETosis was inhibited when the Zn was sequestered by a metal chelator [54]. Evidence also suggested that Zn can cooperate with ROS to exert antibacterial effects, for example, the growth of Zn-sensitive bacterial mutants was significantly inhibited by the presence of both

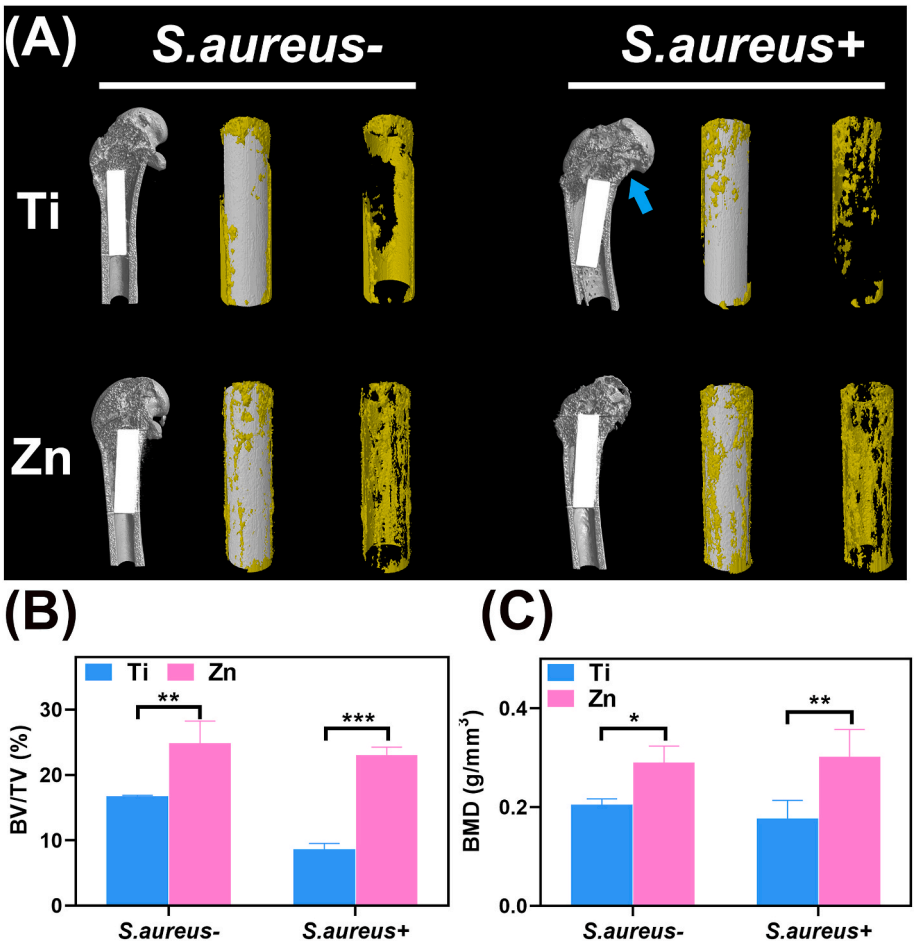

Fig. 8. *In vivo* evaluation of osteogenesis in *S. aureus*-infected and uninfected cases after 2 months. (A) Micro-CT reconstructed images of new bone around the implants (indicated by the yellow section). The blue arrow indicates medullary cavity expansion and cortical bone destruction. The calculated (B) BV/TV and (C) BMD values of the various samples 2 months after implantation (*: $p < 0.05$; **: $p < 0.01$; ***: $p < 0.001$).

Zn and superoxide anions [55]. Recently, studies have indicated that innate immune cells could mobilize Zn and deliver excess Zn^{2+} to intracellular pathogens, and Zn deficiency leads to an increased risk of infection [56,57]; therefore, in addition to its direct antimicrobial impacts, Zn also acts as an antimicrobial effector molecule. Our *in vivo* and *in vitro* experiments confirmed that Zn bulk materials also have an immune-antibacterial effect, and this effect is closely related to oxidative stress.

3.6. Osteogenesis and osseointegration

In vitro cytoskeletal staining was used to illustrate the effect of the material extracts on the morphology of BMSCs. Fig. 7A indicated that the cells were fully spread with the red tensile filaments in the Ti group, while relative shrinkage and poor spreading occurred in the Zn group, consistent with previous study [58]. The corresponding length-width ratio of BMSCs was calculated, and the values for Ti and Zn groups were approximately 4.5 and 2, respectively (Fig. 7B). Literature has reported that, when cultured in osteogenic induction medium, the osteogenesis of MSCs exhibited a non-monotonic change with aspect ratio and the optimal ratio was about 2 [59]. Therefore, in the present study, it was speculated that Zn group is more suitable for osteogenic differentiation. The effects of the material extract on the osteogenic differentiation of BMSCs were then studied by evaluating ALP activity both qualitatively and quantitatively. As shown in Fig. 7C, the darkest and densest purple staining in the Zn group on the 14th day implied the highest ALP expression. As expected, the quantitative ALP activity of the Zn group was also higher than that of Ti ($p < 0.01$; Fig. 7D), indicating the considerable effect of pure Zn on early osteogenesis. Moreover, Ca nodule formation plays an imperative role during the last stage of osteogenesis. ARS staining and concomitant semi-quantitative analysis were performed to evaluate the mineralization efficiency of the Ti and Zn samples. In comparison with the Ti group, the most intensive and extensive area of Ca nodules was found in the Zn group, which was concomitantly validated by semi-quantitative analysis (Fig. 7E and F), suggesting the effectiveness of ECM mineralization. Zn is an essential trace element for skeletal tissue and bone. It is reported that Zn transporter knockout from mice would lead to shorter long bones and dwarfism compared to wildtype mice [60]. Furthermore, Zn ions are widely used as incorporation component to improve implant's osteogenesis [21,23,61]. In particular, a study by Huo et al. reported that a Zn decorated Ti surface could activate ERK1/2 signaling pathway to enhance osteogenesis process [62]. In this work, we also found that the extract containing Zn ions are more favorable for osteogenic differentiation of rBMSCs.

The *in vivo* bone regeneration ability of Zn and Ti implants was evaluated using femur implantation with or without infection. First, the newly formed bone surrounding the implant was reconstructed. Representative Micro-CT images and 3D reconstructions demonstrated a larger area of new bone (Fig. 8A, indicated by yellow) after Zn implanted for 2 months, regardless of whether the bone was infected with *S.aureus* or not. A lower amount of bone was found in the Ti group, with some hollow areas surrounding the implant; however, in the *S.aureus*-infected case, the amount of newly formed bone around the Ti implant decreased

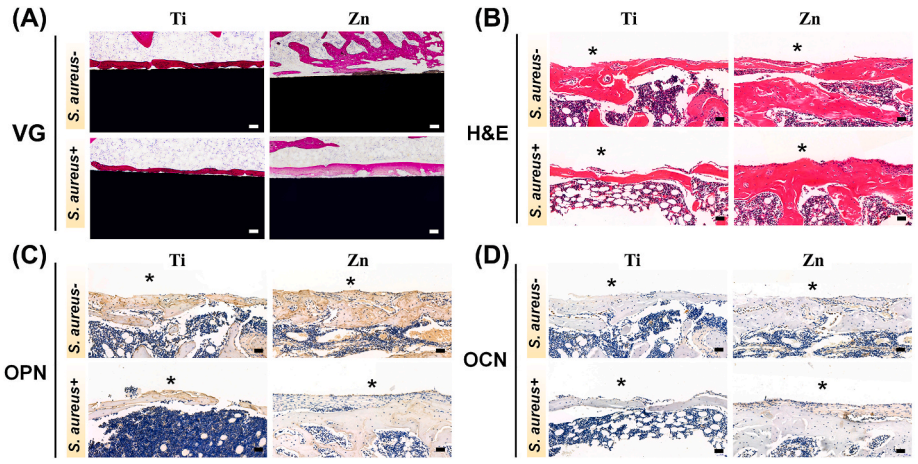

Fig. 9. The histological and immune-histological analysis of decalcified sections around the implants in *S. aureus*-infected and uninfected cases after 2 months. (A) VG staining of various samples 2 months after femur implantation (scale bar = 100 μm). (B) H&E staining of the implant site and thickness of the corresponding new bone (scale bar = 50 μm). Staining of (C) OPN and (D) OCN-positive areas, respectively (scale bar = 50 μm). Asterisks represent the implants.

compared with the uninfected group, presenting as medullary cavity expansion and cortical bone destruction (indicated by the blue arrow). The above results were further confirmed by the corresponding quantification of BV/TV and BMD values around the implants (Fig. 8B and C). Moreover, it was evident that the degradation of pure Zn was not significant after bone implantation within 2 months, regardless of the presence of intraosseous infection.

On the other hand, a histopathological assessment was conducted to analyze the microstructure of new bone around the implants in infected and uninfected states. The results from VG staining of undecalcified bone sections and H&E staining of decalcified bone sections after the samples were implanted for 2 months are shown in Fig. 9A and B, respectively. Both results suggested that the cavities formed around the implants were gradually replaced by newly formed bone tissue. Bone tissue adhered more closely to the surface of Ti implants, but more newly formed bone grew around the Zn implant regardless of *S.aureus* infection. The reason for the discrepancy of H&E results between month 2 and day 3 is that neutrophils around the implants gradually undergo apoptosis after NETs formation and bacterial clearance [63].

Furthermore, bone remodeling activities, manifested by the expression of OCN and OPN, also showed the same trend using immunohistochemical staining, i.e., a more positively stained area (indicated by brown) was observed for the Zn group, both with and without infection (Fig. 9C and D). Zn plays an essential role in bone formation and mineralization. In addition, a proper supply of Zn^{2+} participates in regulating ALP activity and mineralization, which is beneficial for the homeostasis, differentiation, and maturation of osteoblasts [64]. Our *in vitro* and *in vivo* experiments further demonstrated that Zn^{2+} released from Zn implants could regulate osseointegration, even in the presence of *S.aureus* infection, revealing a synergistic effect between antibacterial action and osteogenesis.

4. Conclusion

The immunomodulatory effects of pure Zn on bacterial infection were investigated by focusing on the capture and killing of bacteria by neutrophils. Both *in vitro* and *in vivo* results demonstrated that pure Zn could contribute to the formation of NETs by promoting the release of DNA fibers and granule proteins, thereby binding and killing the invading bacteria; it also resulted in favorable *in vivo* osseointegration during implant-related infection. Results from transcriptome analysis revealed that pure Zn-induced NETs formation was a ROS-dependent process, which involved the activation of NOX, MPO, and PAD4, as well as several inflammatory signaling pathways, such as TLR and cytokine-cytokine receptor signaling pathways. Furthermore, Zn implants exhibited better osteointegration performance than Ti implants in a bone infection model. In summary, these results suggested that Zn and Zn alloys are promising for regulating the immune-antibacterial effects of neutrophils and are suitable for various orthopedic antibacterial implants and devices.

CRediT authorship contribution statement

Feng Peng: Investigation, Data curation, Writing – original draft, Writing – review & editing, Funding acquisition. **Juning Xie:** Investigation, Methodology. **Haiming Liu:** Investigation, Software. **Yufeng Zheng:** Writing – review & editing, Supervision. **Xin Qian:** Investigation, Software. **Hua Zhong:** Writing – review & editing, Supervision. **Yu Zhang:** Supervision, Funding acquisition. **Mei Li:** Investigation, Data curation, Writing – original draft, Writing – review & editing, Funding acquisition.

Declaration of competing interest

The authors declare no conflict of interest.

Acknowledgements

This work was supported by the High-level Hospital Construction Project of GDPH (Grant No. DFJH201905), National Nature Science Foundation of China (Grant No.52271244), Natural Science Foundation of Guangdong Province, China (Grant No. 2022A1515010202), GDPH Supporting Fund for Talent Program (Grant No. KJ012019097, KY0120220137, and KY012021462), GDPH Supporting Fund for NSFC Program (Grant No. KY012021153).

Appendix A. Supplementary data

Supplementary data to this article can be found online at https://doi.org/10.1016/j.bioactmat.2022.09.004.

References

[1] M. Geetha, A.K. Singh, R. Asokamani, A.K. Gogia, Ti based biomaterials, the ultimate choice for orthopaedic implants - a review, Prog. Mater. Sci. 54 (3) (2009) 397–425.
[2] N.A. Hodges, E.M. Sussman, J.P. Stegemann, Aseptic and septic prosthetic joint loosening: impact of biomaterial wear on immune cell function, inflammation, and infection, Biomaterials 278 (2021), 121127.

[3] Y.F. Zheng, X.N. Gu, F. Witte, Biodegradable metals, Mat. Sci. Eng. R 77 (2014) 1–34.
[4] N. Yang, J. Venezuela, S. Almathami, M. Dargusch, Zinc-nutrient element based alloys for absorbable wound closure devices fabrication: current status, challenges, and future prospects, Biomaterials 280 (2022), 121301, 121301.
[5] M.-K. Lee, H. Lee, C. Park, I.-G. Kang, J. Kim, H.-E. Kim, H.-D. Jung, T.-S. Jang, Accelerated biodegradation of iron-based implants via tantalum-implanted surface nanostructures, Bioact. Mater. 9 (2022) 239–250.
[6] H. Yang, B. Jia, Z. Zhang, X. Qu, G. Li, W. Lin, D. Zhu, K. Dai, Y. Zheng, Alloying design of biodegradable zinc as promising bone implants for load-bearing applications, Nat. Commun. 11 (1) (2020) 401.
[7] Y. Yu, H. Lu, J. Sun, Long-term in vivo evolution of high-purity Mg screw degradation - local and systemic effects of Mg degradation products, Acta Biomater. 71 (2018) 215–224.
[8] J.W. Lee, H.S. Han, K.J. Han, J. Park, H. Jeon, M.R. Ok, H.K. Seok, J.P. Ahn, K. E. Lee, D.H. Lee, S.J. Yang, S.Y. Cho, P.R. Cha, H. Kwon, T.H. Nam, J.H. Lo Han, H. J. Rho, K.S. Lee, Y.C. Kim, D. Mantovani, Long-term clinical study and multiscale analysis of in vivo biodegradation mechanism of Mg alloy, P. Natl. Acad. Sci. USA 113 (3) (2016) 716–721.
[9] Y. Qi, H. Qi, Y. He, W. Lin, P. Li, L. Qin, Y. Hu, L. Chen, Q. Liu, H. Sun, Q. Liu, G. Zhang, S. Cui, J. Hu, L. Yu, D. Zhang, J. Ding, Strategy of metal-polymer composite stent to accelerate biodegradation of iron-based biomaterials, Acs Appl. Mater. Inter. 10 (1) (2018) 182–192.
[10] R. Gorejova, L. Haverova, R. Orinakova, A. Orinak, M. Orinak, Recent advancements in Fe-based biodegradable materials for bone repair, J. Mater. Sci. 54 (3) (2019) 1913–1947.
[11] G.K. Levy, J. Goldman, E. Aghion, The prospects of zinc as a structural material for biodegradable implants-A review paper, Metals 7 (10) (2017) 402.
[12] D. Xia, Y. Qin, H. Guo, P. Wen, H. Lin, M. Voshage, J.H. Schleifenbaum, Y. Cheng, Y. Zheng, Additively manufactured pure zinc porous scaffolds for critical-sized bone defects of rabbit femur, Bioact. Mater. 19 (2023) 12–23.
[13] W. Yuan, D. Xia, S. Wu, Y. Zheng, Z. Guan, J.V. Rau, A review on current research status of the surface modification of Zn-based biodegradable metals, Bioact. Mater. 7 (2022) 192–216.
[14] X. Qu, H. Yang, B. Jia, M. Wang, B. Yue, Y. Zheng, K. Dai, Zinc alloy-based bone internal fixation screw with antibacterial and anti-osteolytic properties, Bioact. Mater. 6 (12) (2021) 4607–4624.
[15] R. Wang, Y. Li, Y. Si, F. Wang, Y. Liu, Y. Ma, J. Yu, X. Yin, B. Ding, Rechargeable polyamide-based N-halamine nanofibrous membranes for renewable, high-efficiency, and antibacterial respirators, Nanoscale Adv. 1 (5) (2019) 1948–1956.
[16] H. Kabir, K. Munir, C. Wen, Y. Li, Recent research and progress of biodegradable zinc alloys and composites for biomedical applications: biomechanical and biocorrosion perspectives, Bioact. Mater. 6 (3) (2021) 836–879.
[17] T.K. Fehring, K.A. Fehring, A. Hewlett, C.A. Higuera, J.E. Otero, A.J. Tande, What's new in musculoskeletal infection, J. Bone Joint. Surg. A.M. 103 (14) (2021) 1251–1258.
[18] E.A.-O.X. Masters, B.A.-O. Ricciardi, K.A.-O. Bentley, T.A.-O. Moriarty, E.A.-O. Schwarz, G.A.-O. Muthukrishnan, Skeletal infections: microbial pathogenesis, immunity and clinical management, Nat. Rev. Microbiol. 15 (2022) 1–16.
[19] E. Garcia del Pozo, J. Collazos, J.A. Carton, D. Camporro, V. Asensi, Factors predictive of relapse in adult bacterial osteomyelitis of long bones, BMC Infect. Dis. 18 (1) (2018) 635.
[20] Y. Sun, Y. Zhao, H. Zhang, Y. Rong, R. Yao, Y. Zhang, X. Yao, R. Hang, Corrosion behavior, antibacterial ability, and osteogenic activity of Zn-incorporated Ni-Ti-O nanopore layers on NiTi alloy, J. Mater. Sci. Technol. 97 (2022) 69–78.
[21] F. Peng, D. Wang, D. Zhang, B. Yan, H. Cao, Y. Qiao, X. Liu, PEO/Mg–Zn–Al LDH composite coating on Mg alloy as a Zn/Mg ion-release platform with multifunctions: enhanced corrosion resistance, osteogenic, and antibacterial activities, ACS Biomater. Sci. Eng. 4 (12) (2018) 4112–4121.
[22] X. Chen, B. Tan, S. Wang, R. Tang, Z. Bao, G. Chen, S. Chen, W. Tang, Z. Wang, C. Long, W.W. Lu, D. Yang, L. Bian, S. Peng, Rationally designed protein cross-linked hydrogel for bone regeneration via synergistic release of magnesium and zinc ions, Biomaterials 274 (2021), 120895.
[23] F. Peng, S. Cheng, R. Zhang, M. Li, J. Zhou, D. Wang, Y. Zhang, Zn-contained mussel-inspired film on Mg alloy for inhibiting bacterial infection and promoting bone regeneration, Regen. Biomater. 8 (1) (2021) rbaa044.
[24] X. Xiao, E. Liu, J. Shao, S. Ge, Advances on biodegradable zinc-silver-based alloys for biomedical applications, J. Appl. Biomater. Func. 19 (2021), 22808000211062407.
[25] B. Wang, Y. Li, S. Wang, F. Jia, A. Bian, K. Wang, L. Xie, K. Yan, H. Qiao, H. Lin, J. Lan, Y. Huang, Electrodeposited dopamine/strontium-doped hydroxyapatite composite coating on pure zinc for anti-corrosion, antimicrobial and osteogenesis, Mat. Sci. Eng. C-Mater. 129 (2021), 112387.
[26] Y.H. Zou, J. Wang, L.Y. Cui, R.C. Zeng, Q.Z. Wang, Q.X. Han, J. Qiu, X.B. Chen, D. C. Chen, S.K. Guan, Y.F. Zheng, Corrosion resistance and antibacterial activity of zinc-loaded montmorillonite coatings on biodegradable magnesium alloy AZ31, Acta Biomater. 98 (2019) 196–214.
[27] J.R. Sheldon, E.P. Skaar, Metals as phagocyte antimicrobial effectors, Curr. Opin. Immunol. 60 (2019) 1–9.
[28] K. Ley, H.M. Hoffman, P. Kubes, M.A. Cassatella, A. Zychlinsky, C.C. Hedrick, S. D. Catz, Neutrophils: new insights and open questions, Sci. Immunol. 3 (30) (2018), eaat4579.
[29] V. Thammavongsa, H.K. Kim, D. Missiakas, O. Schneewind, Staphylococcal manipulation of host immune responses, Nat. Rev. Microbiol. 13 (9) (2015) 529–543.
[30] Y. Zhao, Z. Zhang, Z. Pan, Y. Liu, Advanced bioactive nanomaterials for biomedical applications, Explorations 1 (3) (2021), 20210089.
[31] K.A.-O.X. Kienle, K.A.-O. Glaser, S.A.-O. Eickhoff, M.A.-O. Mihlan, K.A.-O. Knöpper, E. Reátegui, M.W. Epple, M.A.-O. Gunzer, R.A.-O. Baumeister, T.A.-O. Tarrant, R.A.-O. Germain, D.A.-O. Irimia, W.A.-O. Kastenmüller, T.A.-O. X. Lämmermann, Neutrophils self-limit swarming to contain bacterial growth in vivo, Science 372 (6548) (2021), eabe7729.
[32] V. Thammavongsa, D.M. Missiakas, O. Schneewind, Staphylococcus aureus degrades neutrophil extracellular traps to promote immune cell death, Science 342 (6160) (2013) 863–866.
[33] Z. Wang, X. Liu, Y. Duan, Y. Huang, Infection microenvironment-related antibacterial nanotherapeutic strategies, Biomaterials 280 (2022), 121249.
[34] F. Binet, G. Cagnone, S. Crespo-Garcia, M. Hata, M. Neault, A. Dejda, M. Wilson Ariel, M. Buscarlet, T. Mawambo Gaelle, P. Howard Joel, R. Diaz-Marin, C. Parinot, V. Guber, F. Pilon, R. Juneau, R. Laflamme, C. Sawchyn, K. Boulay, S. Leclerc, A. Abu-Thuraia, J.-F. Côté, G. Andelfinger, A. Rezende Flavio, F. Sennlaub, J.-S. Joyal, A. Mallette Frédérick, P. Sapieha, Neutrophil extracellular traps target senescent vasculature for tissue remodeling in retinopathy, Science 369 (6506) (2020), eaay5356.
[35] S. Feske, H. Wulff, E.Y. Skolnik, Ion channels in innate and adaptive immunity, Annu. Rev. Immunol. 33 (1) (2015) 291–353.
[36] E.B. Okeke, C. Louttit, C. Fry, A.H. Najafabadi, K. Han, J. Nemzek, J.J. Moon, Inhibition of neutrophil elastase prevents neutrophil extracellular trap formation and rescues mice from endotoxic shock, Biomaterials 238 (2020), 119836.
[37] Y. Maruchi, M. Tsuda, H. Mori, N. Takenaka, T. Gocho, M.A. Huq, N.A.-O. Takeyama, Plasma myeloperoxidase-conjugated DNA level predicts outcomes and organ dysfunction in patients with septic shock, Crit. Care 22 (1) (2018) 176.
[38] V. Brinkmann, C. Reichard U Fau - Goosmann, B. Goosmann C Fau - Fauler, Y. Fauler B Fau - Uhlemann, D.S. Uhlemann, Y. Fau - Weiss, Y. Weiss Ds Fau - Weinrauch, A. Weinrauch, Y. Fau - Zychlinsky, A. Zychlinsky, Neutrophil extracellular traps kill bacteria, Science 303 (5663) (2004) 1532–1535.
[39] L. Yang, Q.A.-O. Liu, X.A.-O. Zhang, X.A.-O. Liu, B.A.-O. Zhou, J. Chen, D. Huang, J. Li, H.A.-O. Li, F. Chen, J. Liu, Y. Xing, X. Chen, S.A.-O. Su, E.A.-O. Song, DNA of neutrophil extracellular traps promotes cancer metastasis via CCDC25, Nature 583 7814 (2020) 133–138.
[40] T. Chavakis, M. Hussain, S.M. Kanse, G. Peters, R.G. Bretzel, J.-I. Flock, M. Herrmann, K.T. Preissner, Staphylococcus aureus extracellular adherence protein serves as anti-inflammatory factor by inhibiting the recruitment of host leukocytes, Nat. Med. 8 (7) (2002) 687–693.
[41] V. Thammavongsa, M. Missiakas Dominique, O. Schneewind, Staphylococcus aureus degrades neutrophil extracellular traps to promote immune cell death, Science 342 (6160) (2013) 863–866.
[42] A. Kuipers, D.A.C. Stapels, L.T. Weerwind, Y.-P. Ko, M. Ruyken, J.C. Lee, K.P. M. van Kessel, S.H.M. Rooijakkers, The Staphylococcus aureus polysaccharide capsule and Efb-dependent fibrinogen shield act in concert to protect against phagocytosis, Microbiology 162 (7) (2016) 1185–1194.
[43] V. Delgado-Rizo, M. Martínez-Guzmán, L. Iñiguez-Gutierrez, A. García-Orozco, A. Alvarado-Navarro, M. Fafutis-Morris, Neutrophil extracellular traps and its implications in inflammation: an overview, Front. Immunol. 8 (2017) 81.
[44] C. Schauer, C. Janko, L.E. Munoz, Y. Zhao, D. Kienhöfer, B. Frey, M. Lell, B. Manger, J. Rech, E. Naschberger, R. Holmdahl, V. Krenn, T. Harrer, I. Jeremic, R. Bilyy, G. Schett, M. Hoffmann, M. Herrmann, Aggregated neutrophil extracellular traps limit inflammation by degrading cytokines and chemokines, Nat. Med. 20 (5) (2014) 511–517.
[45] E.A.-O. Sprenkeler, J. Zandstra, N.A.-O. van Kleef, I. Goetschalckx, B. Verstegen, C. E.M. Aarts, H. Janssen, A.T.J. Tool, G. van Mierlo, R. van Bruggen, I.A.-O. Jongerius, T.W. Kuijpers, S100A8/A9 is a marker for the release of neutrophil extracellular traps and induces neutrophil activation, Cells 11 (2) (2022) 236.
[46] C.C. Winterbourn, A.J. Kettle, M.B. Hampton, Reactive oxygen species and neutrophil function, Annu. Rev. Biochem. 85 (2016) 765–792.
[47] H.R. Thiam, S.A.-O. Wong, R. Qiu, M. Kittisopikul, A. Vahabikashi, A.E. Goldman, R.D. Goldman, D.D. Wagner, C.M. Waterman, NETosis proceeds by cytoskeleton and endomembrane disassembly and PAD4-mediated chromatin decondensation and nuclear envelope rupture, Proc. Natl. Acad. Sci. USA 117 (13) (2020) 7326–7337.
[48] D.N. Douda, M.A. Khan, H. Grasemann, N. Palaniyar, SK3 channel and mitochondrial ROS mediate NADPH oxidase-independent NETosis induced by calcium influx, Proc. Natl. Acad. Sci. USA 112 (9) (2015) 2817–2822.
[49] M.E. Simpson, W.A. Petri Jr., TLR2 as a therapeutic target in bacterial infection, Trends Mol. Med. 26 (8) (2020) 715–717.
[50] D. Azzouz, M.A. Khan, N. Palaniyar, ROS induces NETosis by oxidizing DNA and initiating DNA repair, Cell Death Dis. 7 (1) (2021) 113.
[51] C.A.-O. Henríquez-Olguin, J.A.-O.X. Knudsen, S.H. Raun, Z. Li, E.A.-O. Dalbram, J. A.-O. Treebak, L. Sylow, R.A.-O. Holmdahl, E.A.-O. Richter, E. Jaimovich, T.A.-O. Jensen, Cytosolic ROS production by NADPH oxidase 2 regulates muscle glucose uptake during exercise, Nat. Commun. 10 (1) (2019) 4623.
[52] K.A.-O. Ley, H.M. Hoffman, P.A.-O. Kubes, M.A.-O. Cassatella, A. Zychlinsky, C.A.-O. Hedrick, S.A.-O. Catz, Neutrophils: new insights and open questions, Sci. Immunol. 3 (30) (2018), eaat4579.
[53] M.J. Niemiec, J. De Samber B Fau - Garrevoet, E. Garrevoet J Fau - Vergucht, B. Vergucht E Fau - Vekemans, R. Vekemans B Fau - De Rycke, E. De Rycke R Fau - Björn, L.Björn E. Fau - Sandblad, G. Sandblad L Fau - Wellenreuther, G. Wellenreuther G. Fau - Falkenberg, P.Falkenberg G. Fau - Cloetens, L. Cloetens P Fau - Vincze, C.F.Vincze L. Fau - Urban, C.F. Urban, Trace element landscape of resting and activated human neutrophils on the sub-micrometer level, Metallomics 7 (6) (2015) 996–1010.

[54] R. Hasan, H.Rink L. Fau - Haase, H. Haase, Zinc signals in neutrophil granulocytes are required for the formation of neutrophil extracellular traps, Innate, Immun 19 (3) (2013) 253–264.
[55] C.A.-O. Stocks, M.D. Phan, M.E.S. Achard, N.T.K. Nhu, N.D. Condon, J. A. Gawthorne, A.W. Lo, K.M. Peters, A.G. McEwan, R. Kapetanovic, M.A.-O. Schembri, M.J. Sweet, Uropathogenic Escherichia coli employs both evasion and resistance to subvert innate immune-mediated zinc toxicity for dissemination, Proc. Natl. Acad. Sci. USA 116 (13) (2019) 6341–6350.
[56] Z.R. Lonergan, E.P. Skaar, Nutrient zinc at the host-pathogen interface, Trends Biochem. Sci. 44 (12) (2019) 1041–1056.
[57] J.A.-O. von Pein, C.A.-O. Stocks, M.A.-O. Schembri, R.A.-O. Kapetanovic, M.A.-O. Sweet, An alloy of zinc and innate immunity: Galvanising host defence against infection, Cell Microbiol. 23 (1) (2021), e13268.
[58] B. Jia, H. Yang, Z. Zhang, X. Qu, X. Jia, Q. Wu, Y. Han, Y. Zheng, K. Dai, Biodegradable Zn-Sr alloy for bone regeneration in rat femoral condyle defect model: in vitro and in vivo studies, Bioact. Mater. 6 (6) (2020) 1588–1604.
[59] X. Yao, J. Peng R Fau - Ding, J. Ding, Effects of aspect ratios of stem cells on lineage commitments with and without induction media, Biomaterials 34 (4) (2013) 930–939.
[60] S. Hojyo, T. Fukada, S. Shimoda, W. Ohashi, B.-H. Bin, H. Koseki, T. Hirano, The zinc transporter SLC39A14/ZIP14 controls G-protein coupled receptor-mediated signaling required for systemic growth, PLoS One 6 (3) (2011), e18059.
[61] J.J. Qiu, L. Liu, B.H. Chen, Y.Q. Qiao, H.L. Cao, H.Q. Zhu, X.Y. Liu, Graphene oxide as a dual Zn/Mg ion carrier and release platform: enhanced osteogenic activity and antibacterial properties, J. Mater. Chem. B 6 (13) (2018) 2004–2012.
[62] K. Huo, X. Zhang, H. Wang, L. Zhao, X. Liu, P.K. Chu, Osteogenic activity and antibacterial effects on titanium surfaces modified with Zn-incorporated nanotube arrays, Biomaterials 34 (13) (2013) 3467–3478.
[63] S. Amin Yavari, S.M. Castenmiller, J.A.G. van Strijp, M. Croes, Combating implant infections: shifting focus from bacteria to host, Adv. Mater. 32 (43) (2020), e2002962.
[64] H. Wang, X. Fu, J. Shi, L. Li, J. Sun, X. Zhang, Q. Han, Y.A.-O. Deng, X. Gan, Nutrient element decorated polyetheretherketone implants steer mitochondrial dynamics for boosted diabetic osseointegration, Adv. Sci. 8 (20) (2021), e2101778.